Manipulation of Mechanical Properties of WAAM Deposited ER70S-6 Through Active Cooling

A Thesis
Presented in Partial Fulfillment of the Requirements for the
Degree of Master of Science
with a
Major in Mechanical Engineering
in the
College of Graduate Studies
University of Idaho
by

Andre Corpus

Major Professor: Michael Maughan Ph.D.
Committee Members: Robert Stephens, Ph.D.;
Indrajit Charit, Ph.D.
Department Administrator: Steven Beyerlein, Ph.D.

December 2019

AUTHORIZATION TO SUBMIT THESIS

This Thesis of Andre Corpus, submitted for the degree of Master of Science with a Major in Mechanical Engineering and titled "Manipulation of Mechanical Properties of WAAM Deposited ER70S-6 Through Active Cooling," has been reviewed in final form. Permission, as indicated by the signatures and dates below, is now granted to submit final copies to the College of Graduate Studies for approval.

Major Professor: _____ Date: _____
Michael Maughan, Ph.D.

Committee Members: _____ Date: _____
Robert Stephens, Ph.D.

_____ Date: _____
Indrajit Charit, Ph.D.

Department Administrator: _____ Date: _____
Steven Beyerlein, Ph.D.

ABSTRACT

The purpose of this research was to determine the scope of influence active cooling can have on the mechanical properties of Wire-Arc Additive Manufacturing (WAAM) printed steel. Active cooling is achieved by applying coolant onto deposited material continuously and directly behind the molten puddle. Tensile specimens were cut from thin walls of stacked single width passes. Tensile and hardness tests show the yield strength of ER70S-6 can increase up to 90 KSI and 10 HRC respectively. By employing active cooling methods with a steel-depositing WAAM system we have shown the hardness and yield strength of prints can be manipulated on-the-fly.

For:
Archimedes Tyberius,
Aika Dawn
&
Andromyda Kol Rainier

TABLE OF CONTENTS

LIST OF TABLES

LIST OF FIGURES

1 INTRODUCTION

1.1 ADDITIVE MANUFACTURING

Additive manufacturing (AM), often referred to as 3-D Printing, is increasing in popularity throughout industry. This technology has several distinct advantages over traditional methods: it allows the production of components that are otherwise impossible to manufacture and reduces the cost of manufacturing parts that require special tooling or setup time. AM methods cover an increasingly wide range of materials including plastics, ceramics, metals and even cellular tissue [1].

Metallic AM can be broken down into three categories: powder bed, powder feed and wire feed systems [2].

The basic principle of wire additive manufacturing systems is that a laser, electron beam, or plasma arc creates a pool of molten metal that wire is then fed continuously into, adding material to the structure. There are several varieties of wire feed systems, the bulk of which fall into two categories: gas metal arc welding (GMAW) and gas tungsten arc welding (GTAW) welding systems. The main difference between GMAW and GTAW is that in the GMAW process the feed wire is a current carrying wire that creates the plasma arc, while in the GTAW process a separate tungsten electrode fulfills this function. This research focuses specifically on the GMAW Metal AM process referred to hereafter as Wire Arc Additive Manufacturing or WAAM.

The WAAM process is feasible for all materials that are electrically conductive and can be formed into wire. WAAM processes are the most efficient metallic AM processes with an arc efficiency of about 84% [3]. Arc efficiency describes the ratio of energy transferred to the base material vs energy lost to the surroundings. WAAM processes inherently produce near net shape components which reduces material waste from ~90% as seen in traditional manufacturing processes to less than 10% [4]. This is very desirable when manufacturing components from high value materials such as titanium or difficult to machine materials such as high nickel alloys. WAAM is capable of depositing ten times more material per hour than powder fed methods [4]. The economics of drawing the feed material into wire vs manufacturing metallic powders also gives WAAM an advantage over its powder feed counterparts as wire drawing is much faster and cheaper than making metallic powders.

1.2 CARBON STEELS

There are several microconstituents of a carbon steel compound; austenite, pearlite, bainite and martensite. As a carbon steel is heated above the austenitization temperature it undergoes a phase transformation where it recrystallizes as austenite. As steel is cooled from this elevated temperature it will undergo transformation once again, the final composition of the steel is a function of the starting temperature, the final temperature, and the cooling rate from the starting temperature to the final temperature. This information is shown on an alloy's time temperature transformation diagram (TTT Diagram) as depicted in Figure 1.1. If the material is cooled quickly martensite can be formed which is desirable for its strength and hardness by G. Krauss [5]. Ravikumar et al.[6] showed this very clearly in a study where they investigate the strength and microstructure of carbon steels that were cooled at extremely high rates.

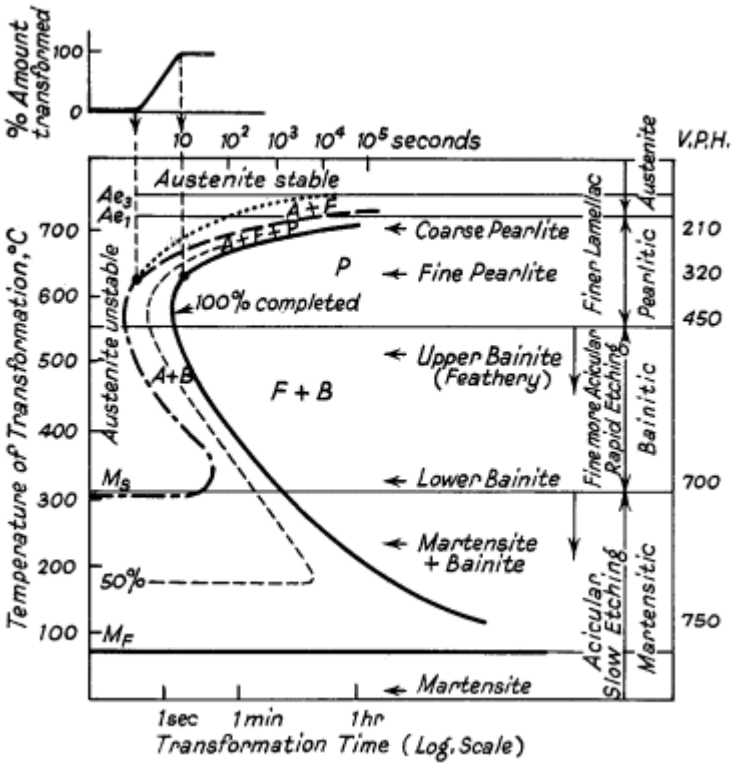

Figure 1.1 - Typical Time Temperature Transformation Diagram

1.3 WAAM Research

Research has been conducted to better understand the properties and microstructure of WAAM deposited material. Baufield et al. [7] created structures of Ti-6Al-4V using an automated welding process documented the properties and microstructure. Other groups have attempted to optimize the WAAM process using a variety techniques [8][9][10] , most of this research surrounds Ti-6Al-4V. Bermingham et al. [11] were able to show that by adding trace amounts of boron into the process they were able to eliminate much of the anisotropy commonly associated with layered additive manufacturing techniques. While researchers are continuing to develop new processes and techniques for WAAM operations focus trends toward processes that develop uniform mechanical properties and microstructure of a printed part.

The present research investigates the next step towards printing components with purpose-built nonuniform mechanical properties and microstructure. This is achieved by combining WAAM technology with the long-understood practice of heat-treating steels. In WAAM, as material is "laid down," the temperature of the deposited material is far above the melting temperature of the base material. Active cooling strategies, such as water spray, to increase the heat transfer rate from deposited material should decrease the cooling time. This decreased cooling time should yield a change in strength and hardness as observed by G. Krauss [5] and Ravikumar et al. [6].

2 EXPERIMENTAL METHODS

2.1 EQUIPMENT

A custom WAAM apparatus developed at the University of Idaho (Vandal Forge) was used as the platform for the present work. The system utilized a commercially available wire feed GMAW system for the deposition of material in the WAAM process. The print area, or bed, is limited to travel in the Y direction while X and Z travel are carried out with a gantry system that controls the print-head motion. Y and Z motion is achieved via stepper motors and lead screws while X motion requires a stepper motor and a belt system. A Smoothie X5 control board flashed with custom firmware commands the stepper motors. GCODE is sent to the control board using a customized version of OctoPrint as the graphical user interface (GUI). A basic flowchart of the system can be seen in Figure 2.3.

A good print cross-section is reasonably hemispherical in shape after it is deposited onto the base material or previous layer. Several parameters effect print quality including current, voltage, gas flow rate, gas type, polarity, wire feed speed, stickout, and print head travel speed. Stickout describes the length of feedwire that is exposed between the contact tip and the base material (See Figure 2.1). The authors' experiments have shown current, travel speed and stickout to have the largest influence on the geometry of the cross-section of deposited metal perpendicular to the direction of travel. Current affects the temperature of the print by increasing or decreasing the power delivered to the system. High current will make a wider, shorter cross-section while lower current will create a taller narrow one. High travel speed will make a tall narrow print while a slow travel speed creates a wide short cross-section. The stickout length influences the power by changing the length of the plasma arc. A larger stickout creates a wider short cross section while a shorter stickout creates a narrow tall one. Current, travel speed and stickout were determined experimentally to create a uniform cross section and are listed in Table 2.1.

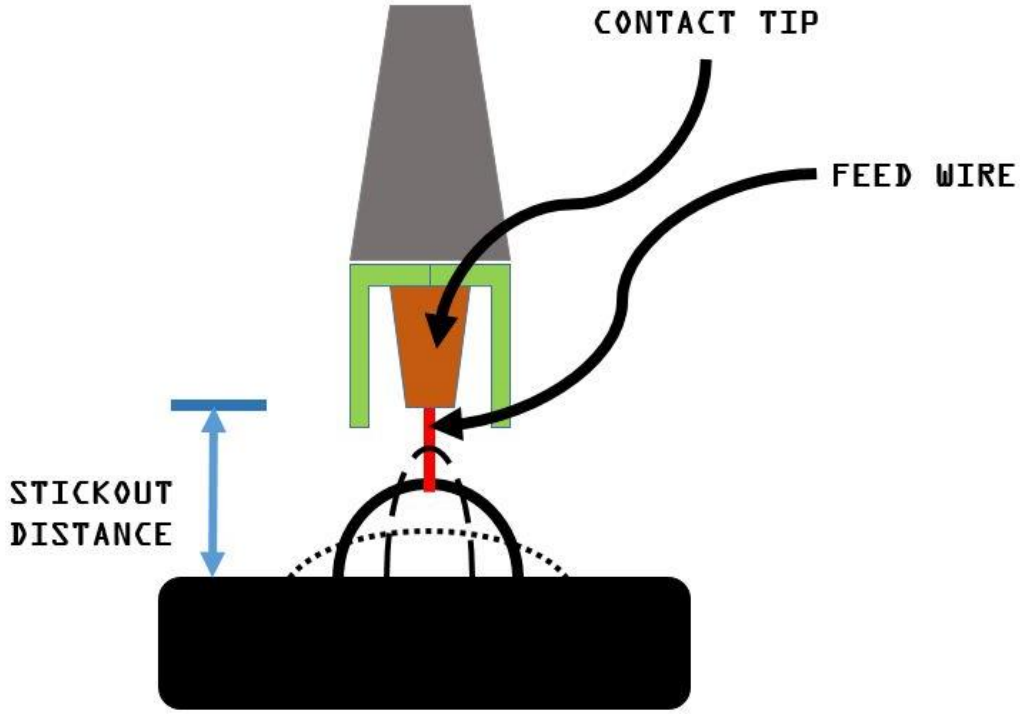

Figure 2.1 - Representation of the contact tip and stickout distance on the Vandal Forge. Wide bead represented by a dotted line and narrow bead represented by dashed line.

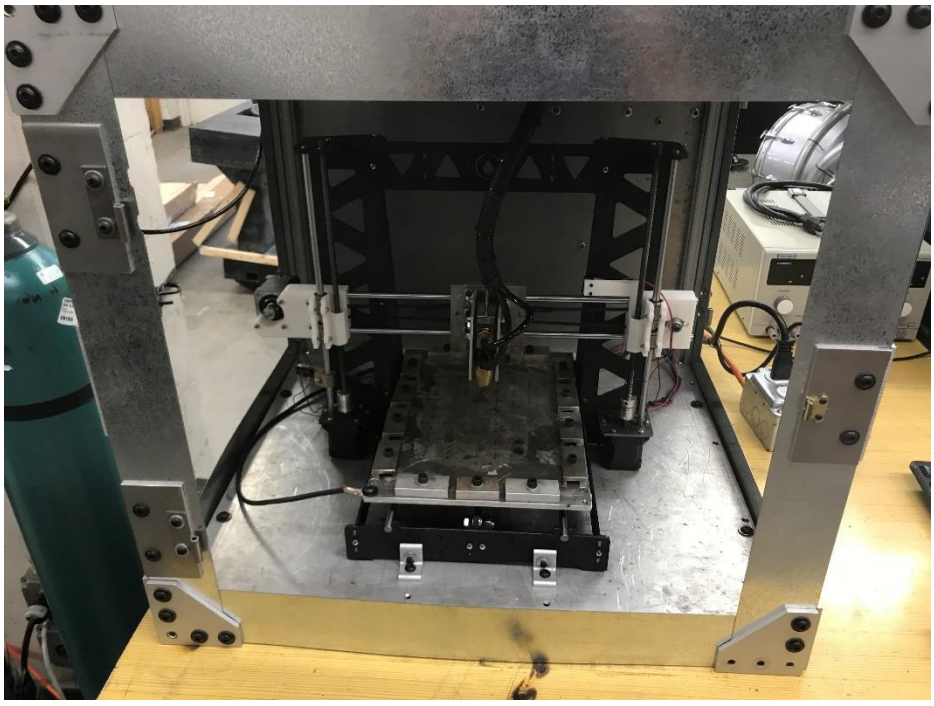

Figure 2.2 - Picture of the Vandal Forge WAAM system

2.2 PRINTING

Thin wall sections of deposited metal were used for testing. 1 in x 5 in x 1/2 in coupons of low carbon hot rolled steel were used as the base material in this experiment. The GCODE for this operation can be found in APPENDIX A: GCODE. The resulting samples were 4 in long, 8 layers (roughly 5/8 in) high and approximately 3/8 in thick. The process variables used for the deposition of all samples are shown in Table 2.1.

Two sample sets were printed: control and test. Control samples consisted of the aforementioned 4 in long printed stacks. Single layers were printed and allowed to cool for approximately 90 seconds before the next layer was printed, the Z-axis was re-zeroed between layers to ensure a 5/16 in stickout was maintained. The 90 second cooling time was essential to avoid deformation caused by excessive heat buildup.

Table 2.1 - System settings for Vandal Forge during testing.

WAAM System Test Settings	
Voltage	30VDC
Current	160A
Wire Size	.023 in
Stickout	5/16 in
Gas Type	60/40 Ar/CO_2
Gas Flow Rate	40 SCFH
Gas Purge Time	1 Second
Polarity	DCEN
Wire Feed Speed	110 ft/min
Print Travel Speed	16 in/min
Wire Type	ER70S-6

Using the same GCODE active cooling was applied to the samples as they were printed. A Kool Mist #60M12 coolant mister was employed to achieve this. Pure argon was used as the carrier gas and tap water as the applied coolant. Flowrate of the argon was set at 40 SCFH (Standard Cubic Feet per Hour) and the flowrate of the tap water was 2.2 in^3/min. Spray cooling trailed the print head 1-1/2 in and was raised 2 in above the print

plane at a 20-30 degree angle from vertical pointing away from the print head (see Figure 2.4). It was found that if the spray cooling was placed closer the force from the spray could deform the material as it was still extremely hot and malleable. The 20-30 degree angle was necessary to keep the spray and steam from disrupting the gas pocket under the print head. It should be noted that it was not necessary to wait the 90 seconds between print layers as the active cooling was able to cool the print to a level that facilitated continuous printing.

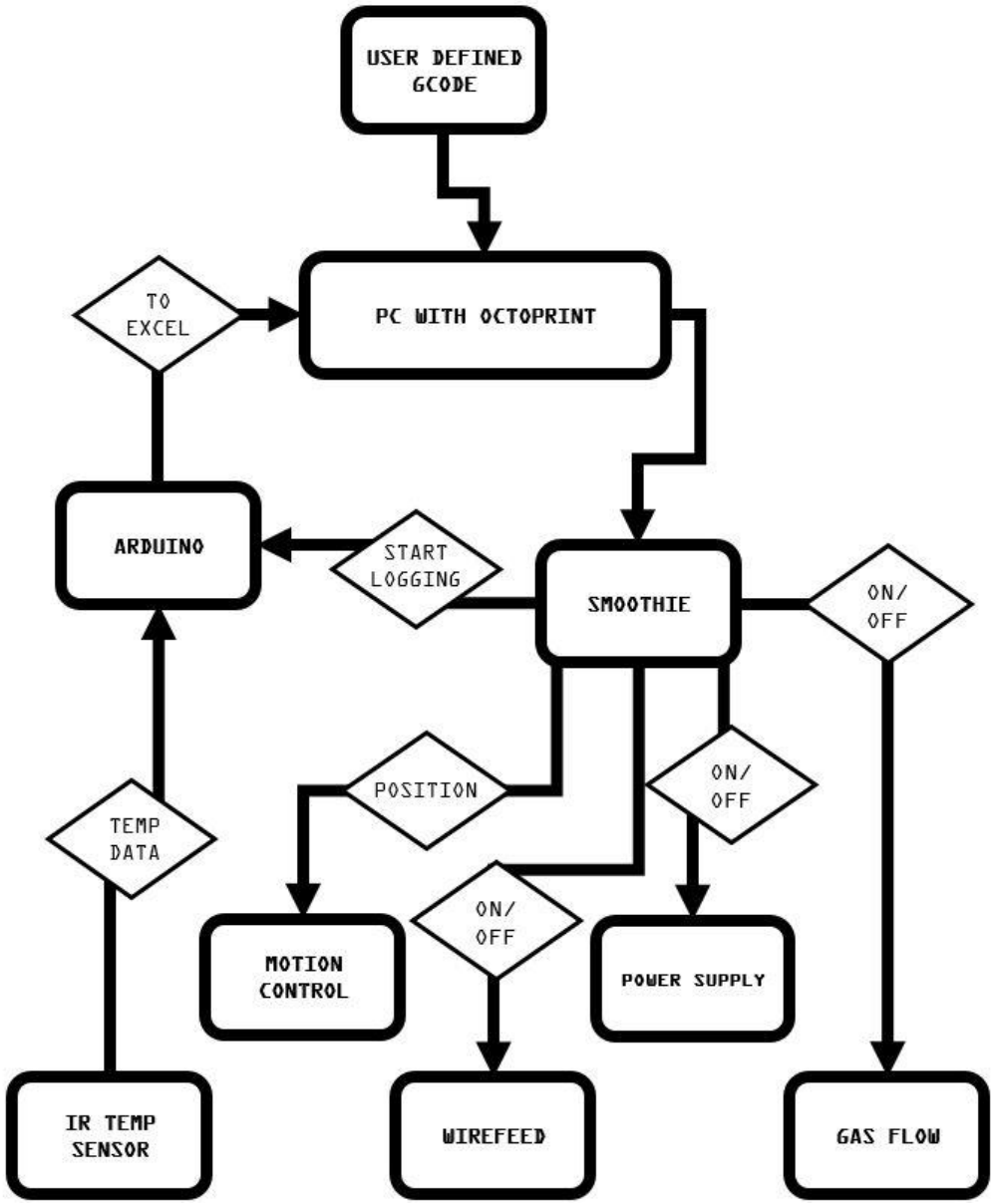

Figure 2.3 - The control schematic for Vandal Forge.

2.3 TESTING

After the prints had all cooled to room temperature, the top surfaces were milled flat with a 1/2 in carbide end mill in preparation for indentation testing. The samples were then polished progressively on a wet platen with 120 grit to 2400 grit silicon carbide paper.

Rockwell Hardness testing was conducted on a Rockwell hardness tester. The hardness tester was checked for accuracy using a 62.5 HRC calibration block. The Rockwell C Scale was used to assess the hardness. Each sample was tested a minimum of 15 times longitudinally along the print.

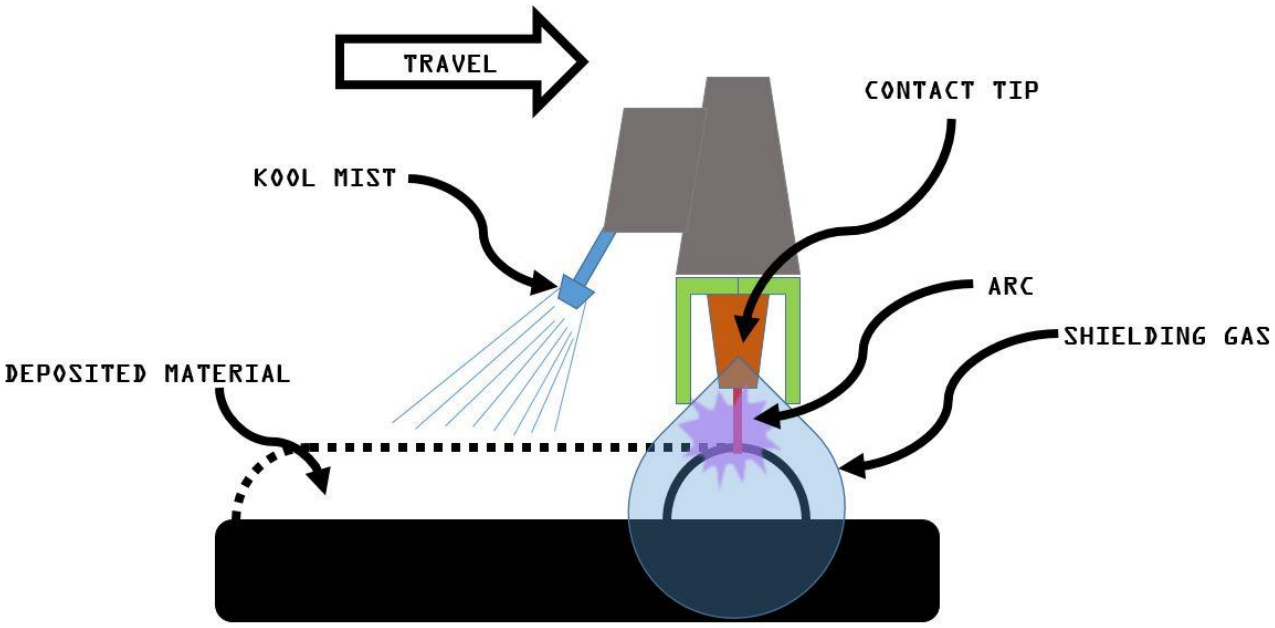

Figure 2.4 - Configuration of the print head on Vandal Forge

Tensile strength was assessed next. Each print was milled down to a single tensile specimen. Sharp edges were broken but specimens were not polished (see Figure 2.5 for reference). Testing was carried out on a SATEC T5000. Specimens were loaded to failure and the ultimate strength was recorded to the nearest 10 lb increment.

Sides of the fractured tensile specimens were ground and polished from 60 grit to 3 micron polishing compound on a wet platen. Samples were then etched with Andre's HomeBrew No. 7 (See APPENDIX B: Etchant for composition). An Olympus PGM-3 microscope was used to capture optical images of the etched microstructure.

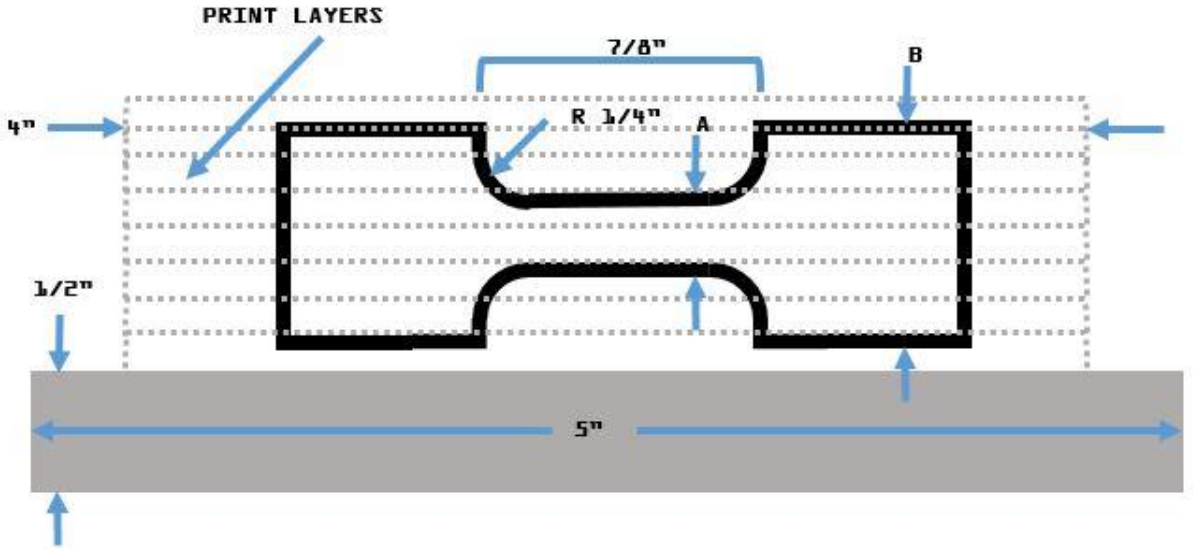

Figure 2.5 - Specimen geometry and location in print. A, B, overall length and thickness vary due to inconsistencies in the print geometry. Prints were milled down to the largest tensile specimen possible.

Percent reduction in area was measured to assess the ductility of specimens. Fractured specimens were measured with digital calipers to .0005 in accuracy near the fracture surface and the percent reduction in area was calculated using Equation 2.1 below.

$$\frac{\text{INITIAL AREA} - \text{FINAL AREA}}{\text{INITIAL AREA}} \times 100 = \text{PERCENT REDUCTION IN AREA}$$

Equation 2.1 - Formula used for calculating the percent reduction in area

3 RESULTS

3.1 HARDNESS TESTING

The control group averaged a HRC of 30.5 with a standard deviation of 1.3. There was a high of 32.5 and a low of 24.5 over 107 sample sites. The test group averaged an HRC of 38.3 with a standard deviation of 1.6. There was a high of 41 and a low of 36 over 79 test sites.

3.2 TENSILE TESTING

Tensile tests for the control group yield an ultimate strength (UTS) that ranges from 64.6 KSI to 93.6 KSI with an average of 80.35 KSI as shown in Table 3.1.

Table 3.1 - Ultimate tensile strength data for the control group.

CONTROL GROUP

SAMPLE	UTS [KSI]	AREA [in^2]	FORCE [lbf]
1	93.60	0.025	2340
2	64.60	0.02415	1560
3	80.16	0.0378	3030
4	81.22	0.017115	1390
5	82.19	0.021658	1780
AVG	80.35		

Tensile tests for the test group show ultimate strength ranges from 106.28 KSI to 172.06 KSI with an average of 144.75 KSI as shown in Table 3.2. It should be noted that Sample No. 2 had major porosity as show in Figure 3.1. This porosity is assumed to be the reason for the lower than normal UTS as most samples had a very uniform cross section with no voids or porosity.

Table 3.2 - Ultimate tensile strength data for the test group.

TEST GROUP

SAMPLE	UTS [KSI]	AREA [in^2]	FORCE [lbf]
1	172.06	0.01947	3350
2	106.28	0.01976	2100
3	154.95	0.018522	2870
4	150.03	0.011398	1710
5	140.42	0.016095	2260
AVG	144.75		

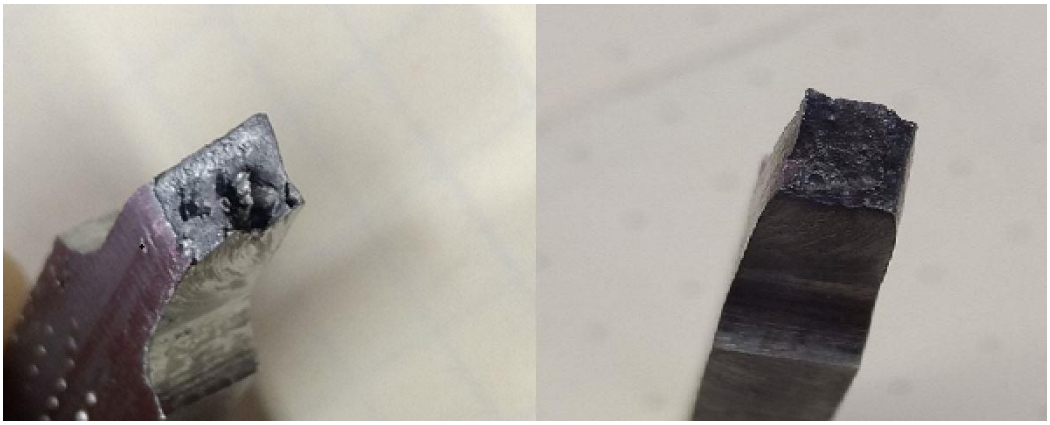

Figure 3.1 - Image of the porosity in test sample No. 2 (left) and a good sample with no porosity (right)

3.3 REDUCION IN AREA

Ductility was assessed using percent reduction area (RA). RA of the control group showed an average RA of 37%, with a high of 49% and a low of 29%. The test group showed an average RA of 7% with a high of 12% and a low of 3%. Data for RA measurements can be seen in Table 3.3.

Table 3.3 - Percent Reduction Area of all samples.

CONTROL GROUP	
SAMPLE	% REDUCTION AREA
1	39%
2	29%
3	29%
4	49%
5	38%
AVG	37%

TEST GROUP	
SAMPLE	% REDUCTION AREA
1	3%
2	12%
3	6%
4	5%
5	7%
AVG	7%

3.4 RELATIONSHIP OF MATERIAL PROPERTIES

It is well-known and understood that most of a material's mechanical properties are related. Optimizing one property is often at the compromise of another. Not surprisingly, the results of this research align well with what has been seen by scientists of today and yesteryear. Strength and hardness have a direct relationship: as one increases the other also

increases with it. Consequently, strength and ductility have an inverse relationship: as strength increases ductility decreases. Figure 3.2 shows the fractures of typical control samples (top) and a test samples (bottom).

Figure 3.2 - Fracture surfaces of tensile specimens, control sample (top) test sample (Bottom).

It is requisite to note the correlation between hardness, strength and ductility. By understanding how material properties are intertwined, it becomes possible to engineer materials for specific tasks. By evaluating the data from this experiment, limitations and expectations for printed materials can be established. Understanding the capabilities of this WAAM system will allow for production of components that are designed and engineered to accomplish specific tasks.

3.5 TYPICAL VALUES

Typical values for hardness, UTS and ductility of common AISI steels can be found in APPENDIX C: AISI Steel Properties.

4 ANALYSIS

4.1 MICROSTRUCTURE

Optical microscopy was used to evaluate the state of the microstructure of the samples. The samples were visually compared to micrographs of material with a known composition. The microstructure of air cooled AISI 1008 as seen by Ravikumar et al [6, Fig. 3] can be seen in Figure 4.1 which clearly shows the phase composition to be ferrite and pearlite. Figure 4.2 shows the typical microstructure of the control prints in this experiment. The microstructure of the control print from this experiment shows a high degree of similarity with the air-cooled sample seen by Ravikumar et al. Similarities include grain shape, size and the general texture of the matrix (larger ferrite grains in white with pearlite clusters at the grain boundaries). It is therefore logical to assume the phase composition of the control sample to be ferrite and pearlite as well.

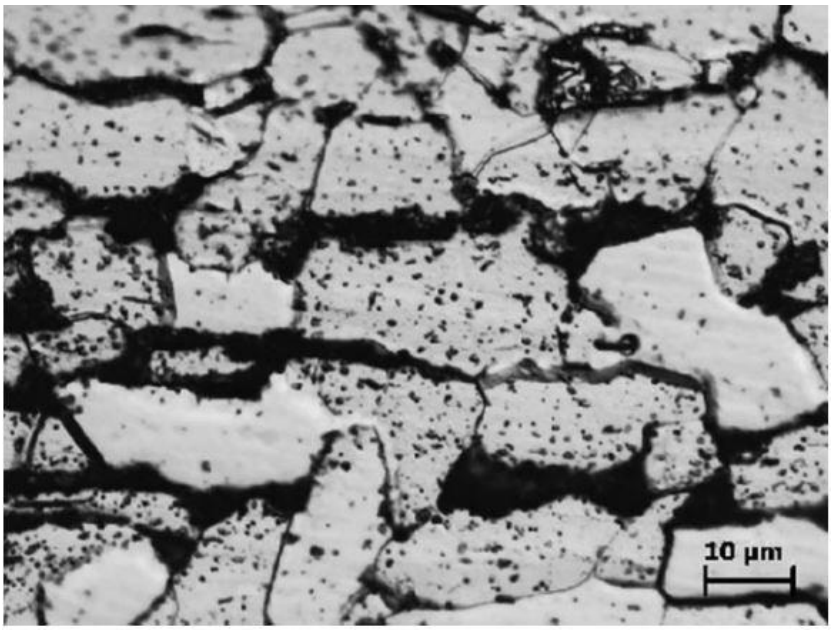

Figure 4.1 - Ferrite and pearlite microstructure of the air cooled samples from Ravikumar et al [6, Fig. 3].

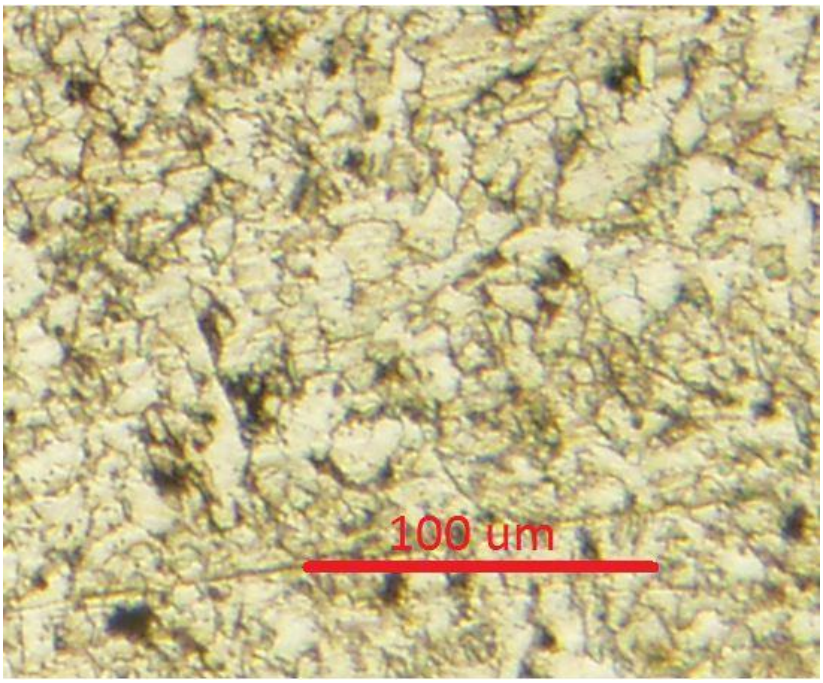

Figure 4.2 - Ferrite and pearlite microstructure of the control print samples.

Ravikumar et al. showed the microstructure of AISI 1008 at an accelerated cooling rate of 332 °F/s in Figure 4.3, which clearly has a primary phase composition of lath martensite. Figure 4.4 shows the typical microstructure of the test prints in this experiment, this sample shows major similarities with the cooled AISI 1008 [6, Fig. 15B]. The erratic jagged stacked needle-like structure can be easily identified in both samples. It is therefore logical to assume that the test sample of this experiment is primarily composed of lath martensite.

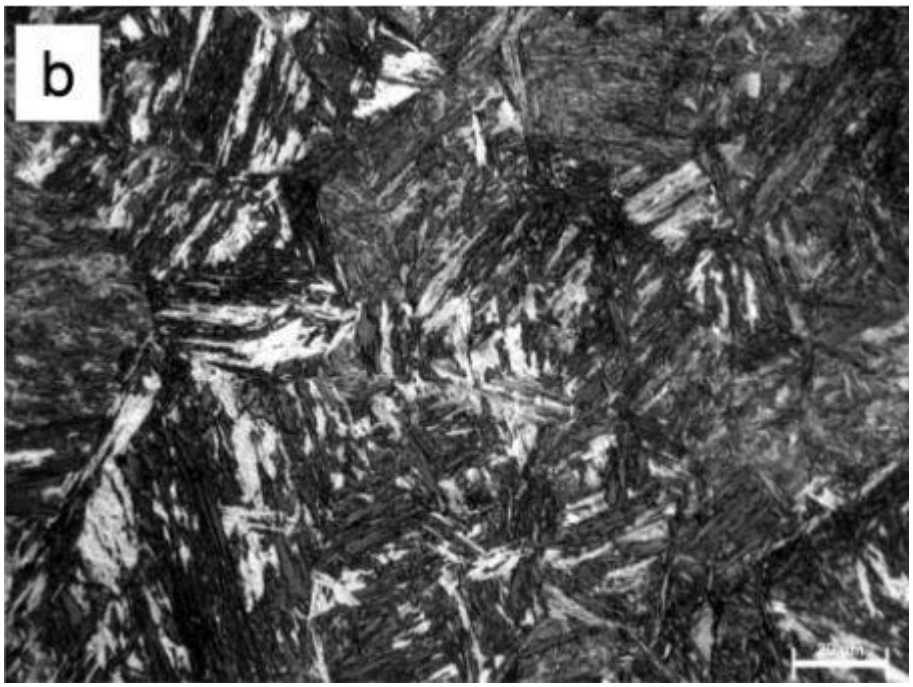

Figure 4.3 - Lath martensite microstructure of the cooled samples from Ravikumar et al. [6, Fig. 15B].

Figure 4.4 - Lath martensite microstructure of the test samples.

4.2 COOLING RATE CORRELATIONS

The results presented in the previous section show that the application of misted water as a cooling agent during the print cycle can have a significant impact on the material properties of the print. The hardness of the treated samples increased almost 8 HRC, the average strength of the treated samples increased 180% and the percent RA decreased from 37% to 7%. Given the tabulated data and the micrographs in this section, the increase in strength and hardness can be primarily attributed to the formation of martensite.

Figure 4.5 shows graphs of cooling rate vs. strength and hardness which illustrate a very linear relationship [6, Fig. 21,22]. It should be noted that the findings of this research differ slightly from the results by Ravikumar et al. AISI 1008 is often used as a comparison to ER70S-6 welding wire as they have similar carbon content, however ER70S-6 has several elements not present in AISI 1008. The increased strength and hardness observed in this research is attributed to this fact. Composition of the two materials can be found in APPENDIX D: Material Composition

.

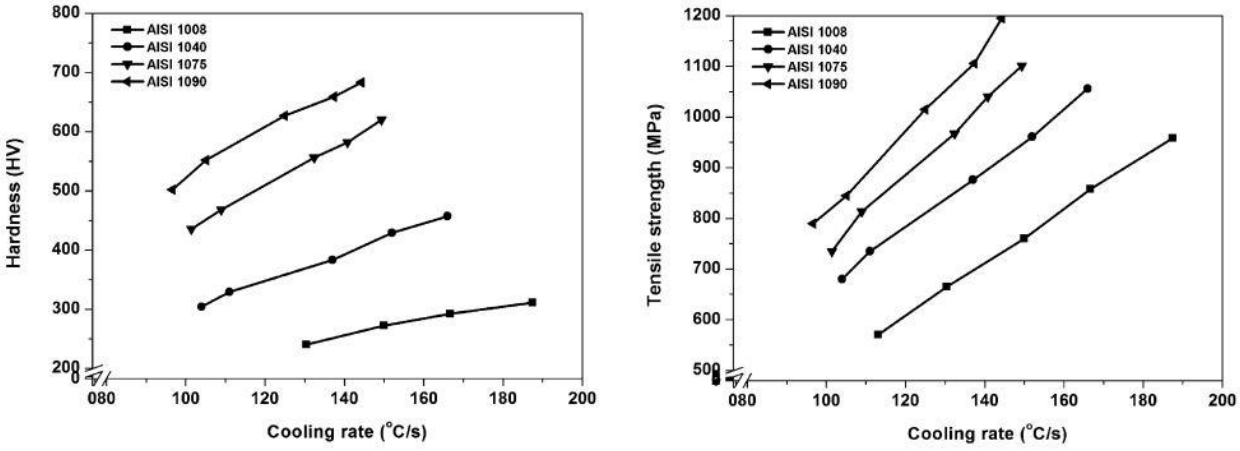

Figure 4.5 - Cooling rate graphs [6, Fig. 21,22].

If the relationships portrayed in Figure 4.5 are assumed to be linear the construction of a simple model that can correlate flow rate of misted water to the final hardness and strength of printed components becomes possible. A Micro Epsilon IMH1-CF2-CB3 was used to measure the cooling rate of the samples in situ with and without cooling. Due to the current state of the testing apparatus the coolant spray is Boolean with a flow rate of 2.2 in^3/min or no coolant.

Figure 4.6 shows the cooling rate for maximum flow and no flow. It has been shown that the flow of atomized water spray used for cooling low carbon steel is directly related to the cooling rate, and this relationship shows good linearity as seen in Figure 4.7 [6, Fig. 14].

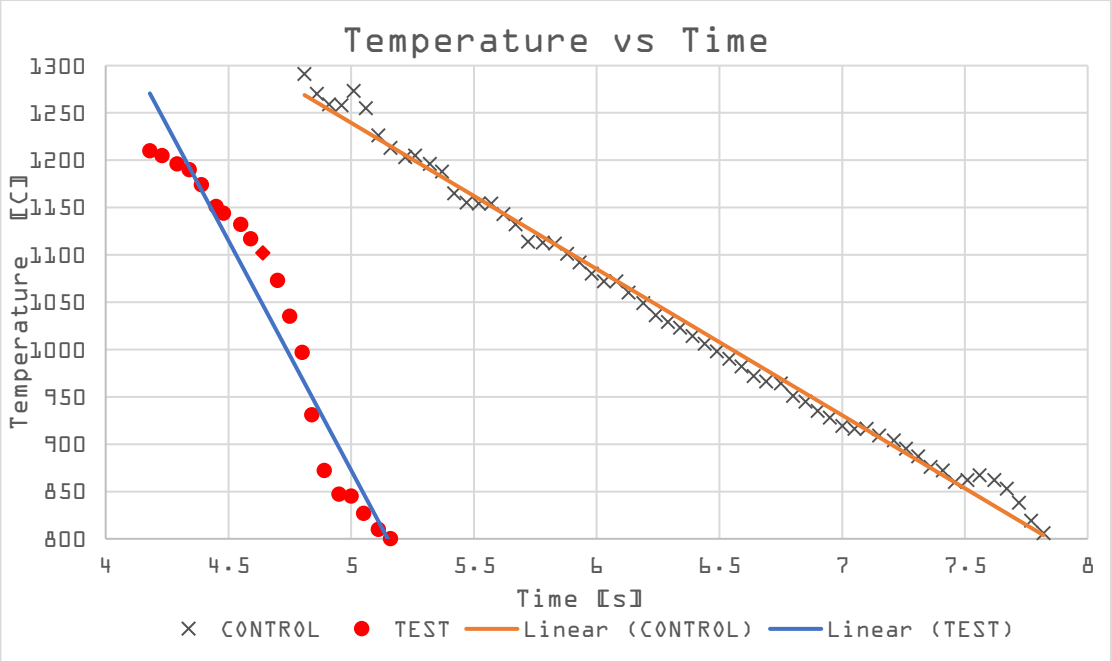

Figure 4.6 - Vandal Forge temp v time data, with cooling and without.

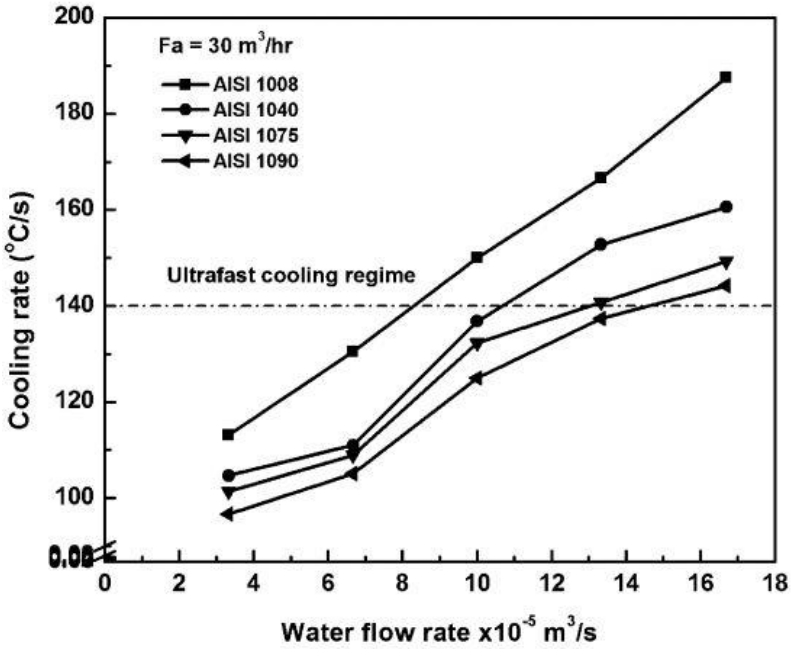

Figure 4.7 - Cooling rate vs. flow rate of atomized water spray [6, Fig. 14].

From this relationship we can develop a model that will work with the Vandal Forge to selectively print material with specific properties. Compiling data from Ravikumar et al. with data collected on the Vandal Forge we can build a table that would predict the mechanical properties of printed material if based off the flow rate of water cooling applied to the print. Table 4.1 shows values that could be programmed into the Vandal Forge software to produce prints with varying material properties.

Table 4.1 - Flow rate vs HRC and UTS correlation for Vandal Forge

Coolant Flow rate [in^3/min]	HRC	UTS [KSI]
0	30	80
0.22	31	89.2
0.44	32	98.4
0.66	33	107.6
0.88	34	116.8
1.1	35	126
1.32	36	135.2
1.54	37	144.4
1.76	38	153.6
1.98	39	162.8
2.2	40	172

5 CONCLUSIONS

In this experiment the effects of spray water cooling of ER70S-6 welding wire during a print was investigated. This was achieved by spraying printed material with atomized water immediately after its deposition. Hardness testing showed an increase in the HRC hardness of printed specimens up to 10 points higher than the control group average. Tensile tests also showed an increase in strength of 90 KSI over the control group average. It has been shown that active cooling immediately after a WAAM process is a viable way to manipulate the hardness and strength of a 3-D printed component. Investigating the correlation between coolant flow rate, cooling rate and the mechanical properties has led to the development of a table that can be used to predict the hardness and strength of printed material using coolant flow rate as an input.

6 REFERENCES

[1] X. Lu, Y. F. Zhou, X. L. Xing, L. Y. Shao, Q. X. Yang, and S. Y. Gao, "Open-source wire and arc additive manufacturing system: formability, microstructures, and mechanical properties," *The International Journal of Advanced Manufacturing Technology*, vol. 93, no. 5-8, pp. 2145-2154, Nov. 2017.

[2] W. E. Frazier, "Metal Additive Manufacturing: A Review," *Journal of Materials Engineering and Performance*, vol. 23, no. 6, pp. 1917-1928, Jun. 2014.

[3] J. N. DuPont and A. R. Marder, "Thermal efficiency of arc welding processes," *Welding Journal-Including Welding Research Supplement*, vol. 74, no. 12, p. 406s, 1995.

[4] A. Busachi, J. Erkoyuncu, P. Colegrove, F. Martina, and J. Ding, "Designing a WAAM Based Manufacturing System for Defence Applications," *Procedia CIRP*, vol. 37, pp. 48-53, 2015.

[5] G. Krauss, "Martensite in steel: strength and structure," *Materials science and engineering: A*, vol. 273, pp. 40-57, 1999.

[6] S. V. Ravikumar, J. M. Jha, S. S. Mohapatra, S. K. Pal, and S. Chakraborty, "Influence of Ultrafast Cooling on Microstructure and Mechanical Properties of Steel," *steel research international*, vol. 84, no. 11, pp. 1157-1170, Nov. 2013.

[7] B. Baufeld, O. V. der Biest, and R. Gault, "Additive manufacturing of Ti-6Al-4V components by shaped metal deposition: Microstructure and mechanical properties," *Materials & Design*, vol. 31, pp. S106-S111, Jun. 2010.

[8] J. Ding *et al.*, "Thermo-mechanical analysis of Wire and Arc Additive Layer Manufacturing process on large multi-layer parts," *Computational Materials Science*, Jul. 2011.

[9] H. Geng, J. Li, J. Xiong, X. Lin, and F. Zhang, "Optimization of wire feed for GTAW based additive manufacturing," *Journal of Materials Processing Technology*, vol. 243, pp. 40-47, May 2017.

[10] Q. Wu, Z. Ma, G. Chen, C. Liu, D. Ma, and S. Ma, "Obtaining fine microstructure and unsupported overhangs by low heat input pulse arc additive manufacturing," *Journal of Manufacturing Processes*, vol. 27, pp. 198-206, Jun. 2017.

[11] M. J. Bermingham, D. Kent, H. Zhan, D. H. StJohn, and M. S. Dargusch, "Controlling the microstructure and properties of wire arc additive manufactured Ti-6Al-4V with trace boron additions," *Acta Materialia*, vol. 91, pp. 289-303, Jun. 2015.

APPENDIX A: GCODE

```
G21                             ;metric values
G90                             ;absolute positioning
;G28                            ;home all axes

;LINE TEST

G0 F4000 X0 Y0                  ;defines the travel speed and start position (arc will be started at this point)
G0 F4000 Z12                    ;defines the stickout for the first layer
M770                            ;open gas flow solenoid valve
G4 S3                           ;dwell for 3 seconds to purge air from weld environment
M701                            ;enable temperature recording (PLX DAQ Arduino)
M710                            ;turn welder relay pin on
G4 P100                         ;dwell for 100 milliseconds to give welder relay time to actuate
M750 S100                       ;turn on wire feed motor, S represents percent (ex: S75 = 75% max wire feed)
; G4 P0                         ;dwell time for high speed prints (over 3000)
G1 F400                         ;set the print speed

G1                              ;print path
X50 Y0

M400                            ;wait for queue to empty: m-codes below will activate prematurely without this
G4 P100                         ;dwell for 100 milliseconds
M720                            ;turn welder relay pin off
M760                            ;turn off wire feed motor
M780                            ;close gas flow solenoid valve
G4 S5                           ;wait for 5 seconds
M702                            ;disable temperature recording (PLX DAQ Arduino)
G0 Z15                          ;lift print head
```

APPENDIX B: Etchant

Andre's HomeBrew No.7:

-10mL HCL

-1000mL DI H_2O

-2g sodium metabisulfite

APPENDIX C: AISI Steel Properties

AISI	Condition	UTS (KSI)	Elongation (%)	Brinell Hardness (Rockwell C) (Rockwell B)
1015	Hot Rolled	61	39	126
	Normalized	61.5	37	121
	Annealed	56	37	111 (65.7)
1020	Hot Rolled	65	36	143
	Normalized	64	35.8	131
	Annealed	57.3	36.5	111
1022	Hot Rolled	73	35	149
	Normalized	70	34	143
	Annealed	65.3	35	137 (76.4)
1030	Hot Rolled	80	32	179
	Normalized	75	32	149
	Annealed	67.3	31.2	126 (72)
1040	Hot Rolled	90	25	201 (16)
	Normalized	85.5	28	170
	Annealed	75.3	30.2	149
1050	Hot Rolled	105	20	229 (20.5)
	Normalized	108.5	20	217
	Annealed	92.3	23.7	187
1060	Hot Rolled	118	17	241 (22.8)
	Normalized	112.5	18	229
	Annealed	90.8	22.5	179
1080	Hot Rolled	140	12	293 (30.9)
	Normalized	146.5	11	293
	Annealed	89.3	24.7	174
1095	Hot Rolled	140	9	293
	Normalized	147	9.5	293
	Annealed	95.3	13	192

APPENDIX D: Material Composition

ER70S-6:

C = .06 - .15
Mn = 1.4 - 1.85
Si = .8 - 1.15
P = .025 MAX
S = .035 MAX
NI = .15 MAX
Cr = .15 MAX
Mo = .15 MAX
V = .03 MAX
Cu = .5 MAX
Fe = Balance

AISI 1008:

C = .1
Mn = .3 - .5
Fe = Balance
P = .03 MAX
S = .05 MAX